Probabilistic imaginary-time evolution algorithm based on nonunitary quantum circuits

Hao-Nan Xie,[1,2] Shi-Jie Wei,[2,*] Fan Yang,[1,2] Zheng-An Wang,[2] Chi-Tong Chen,[3,4] Heng Fan,[3,2] and Gui-Lu Long[1,2,5,6,†]

[1]*State Key Laboratory of Low-Dimensional Quantum Physics and Department of Physics, Tsinghua University, Beijing 100084, China*
[2]*Beijing Academy of Quantum Information Sciences, Beijing 100193, China*
[3]*Institute of Physics, Chinese Academy of Sciences, Beijing 100190, China*
[4]*School of Physical Sciences, University of Chinese Academy of Sciences, Beijing 100190, China*
[5]*Beijing National Research Center for Information Science and Technology and School of Information, Tsinghua University, Beijing 100084, China*
[6]*Frontier Science Center for Quantum Information, Beijing 100084, China*

(Received 21 December 2022; accepted 4 March 2024; published 9 May 2024)

Imaginary-time evolution is a powerful tool in the study of quantum physics. However, existing classical algorithms for simulating imaginary-time evolution suffer from high computational complexity as the dimension of the quantum system increases. In this study we propose a quantum algorithm for implementing imaginary-time evolution using nonunitary quantum circuits with one ancillary qubit. The success probability of our algorithm is a polynomial function of the output error and can be enhanced by reorganizing the terms of the Hamiltonian. To illustrate the practicality of our algorithm on current quantum devices, we conduct a demonstration on superconducting and trapped-ion quantum processors to calculate the ground-state energy and determine the most stable molecular structure of H_2. Additionally, we validate the feasibility of our algorithm by numerically simulating the ground-state energies of LiH molecules and the quantum Ising chain. In contrast to existing algorithms, our method provides a systematic approach to construct the required nonunitary circuits using universal quantum gates, making it suitable for experimental implementation. Our algorithm opens up possibilities for exploring other physical phenomena such as finite-temperature properties and non-Hermitian systems.

DOI: 10.1103/PhysRevA.109.052414

I. INTRODUCTION

As a valuable mathematical tool, imaginary-time evolution (ITE) finds applications in various quantum physics problems, including the computation of ground states of Hamiltonians [1–3], the investigation of finite-temperature properties [4–7], and the simulation of non-Hermitian systems [8,9]. The concept of ITE can be grasped by introducing an imaginary time $\beta = it$ and substituting it into the Schrödinger equation $i\partial_t |\Phi\rangle = \mathcal{H} |\Phi\rangle$, where $\mathcal{H}$ represents a Hermitian Hamiltonian. This substitution leads to the imaginary-time Schrödinger equation, which can be expressed as follows:

$$-\partial_\beta |\Phi_\beta\rangle = \mathcal{H} |\Phi_\beta\rangle . \tag{1}$$

Given an initial state $|\Phi_0\rangle$, the solution to Eq. (1) is $\Phi_\beta = e^{-\beta\mathcal{H}} |\Phi_0\rangle$, which represents a subnormalized quantum state. The corresponding evolution operator $e^{-\beta\mathcal{H}}$ is nonunitary and the evolved state can be expressed using a normalization constant A as $|\Phi_\beta\rangle = Ae^{-\beta\mathcal{H}} |\Phi_0\rangle$. In classical simulations, one can directly calculate $e^{-\beta\mathcal{H}}$ and implement it on the initial state vector $|\Phi_0\rangle$ or employ other classical techniques such as quantum Monte Carlo [10] and tensor networks [11,12]. However, the dimension of the Hilbert space grows exponentially with the size of the quantum system, making the tasks intractable for classical computers [13].

A quantum computer is one of the promising tools for efficiently simulating quantum systems [13–24]. For real-time simulation, the evolution operator $e^{-it\mathcal{H}}$ can be realized directly or simply decomposed into a sequence of unitary quantum gates. However, this is not possible for imaginary-time simulation, where the evolution operator $e^{-\beta\mathcal{H}}$ is nonunitary. Two types of classical-quantum hybrid algorithms have been proposed to simulate ITE. The first is variational quantum algorithms (VQAs) [25–30], which utilize a variational ansatz to simulate the evolution of quantum states by updating variational parameters with a classical optimizer; however, estimating the complexity of VQAs is still a difficult problem [31,32] and the fixed parametrization of VQAs causes systematic errors. The second hybrid algorithm is quantum imaginary-time evolution [33–35], which identifies a unitary operator to approximate the ideal ITE by solving a group of linear equations in each evolution step. Quantum imaginary-time evolution is suitable for Hamiltonians that contain only local interactions because global correlation will boost the computation complexity [3,35].

Alternatively, nonunitary quantum circuits [36] have broadened the scope of quantum computation. One method to implement nonunitary quantum circuits is the linear combination of unitary operators [37], which has been applied in

*weisj@baqis.ac.cn
†gllong@mail.tsinghua.edu.cn

many problems, such as the full quantum eigensolver [38,39] and Hamiltonian simulation [40,41]. Another method is quantum signal processing [42–44], which implements matrix functions with optimal quantum control sequence controlled by an ancillary qubit. Based on nonunitary circuits, many imaginary-time simulation approaches [3,9,45,46] have been proposed. These studies presented abstract representations of the required unitary gates and provided examples of the circuit construction for two- and three-qubit cases. However, no method has been proposed for more general cases to efficiently decompose the required quantum circuits into universal quantum gates.

In this study we propose a probabilistic imaginary-time evolution (PITE) algorithm that utilizes nonunitary quantum circuits with one ancillary qubit. Compared to the previous studies, we explicitly illustrate the construction of the required quantum circuits using single-qubit and two-qubit gates, which applies to any number of qubits and any Hamiltonians that can be efficiently expressed as a sum of Pauli terms. A detailed analysis of the computational complexity is also provided, where the final success probability of the measurement is a polynomial of the output error. We demonstrate our algorithm by determining the ground state of H_2 on both superconducting and trapped-ion cloud platforms. Furthermore, numerical calculations are performed to determine the ground-state energy of LiH molecules and the quantum Ising chain. In addition, a generalized version of PITE (GPITE) is introduced, which can be applied to more generic Hamiltonians and exhibits better performance in terms of the success probability.

This paper is organized as follows. In Sec. II we provide a description of the PITE algorithm and the analysis of the success probability and the error. Section III presents the results on quantum cloud platforms and numerical simulation results of explicit examples. In Sec. IV we provide the details of the GPITE algorithm. A summary is given and our results are discussed in Sec. V.

II. METHOD

An n-qubit Hamiltonian $\mathcal{H} = \sum_{k=1}^{m} c_k h_k$ is composed of m Pauli product terms, in which c_k is a real coefficient and $h_k = \otimes_{j=1}^{n} \sigma_{\alpha_j}^j$, where $\sigma_{\alpha_j}^j$ is a Pauli matrix or the identity acting on the jth qubit, with $\alpha_j \in \{0, x, y, z\}$ ($\sigma_0 = I$). Here we assume m is on the order of poly(n), and the Hamiltonian does not contain the identity term $I^{\otimes n}$ because this term merely shifts the spectrum of the Hamiltonian.

Our goal is to implement the nonunitary operator $e^{-\beta\mathcal{H}}$ in quantum circuits. We first apply the Trotter decomposition [47,48]

$$e^{-\beta\mathcal{H}} = (e^{-c_1 h_1 \Delta\tau} \cdots e^{-c_m h_m \Delta\tau})^{\beta/\Delta\tau} + O(\Delta\tau). \tag{2}$$

For a single Trotter step, we wish to obtain $|\Phi'\rangle = \tilde{T}_k |\Phi\rangle$, where $\tilde{T}_k = e^{-c_k h_k \Delta\tau}$. Since $c_k h_k$ only has two different eigenvalues $\pm|c_k|$, each with the degeneracy of 2^{n-1}, there exists a unitary U_k satisfying

$$U_k c_k h_k U_k^\dagger = -|c_k| \sigma_z^{l_k}, \quad l_k \in \{1, \ldots, n\}, \tag{3}$$

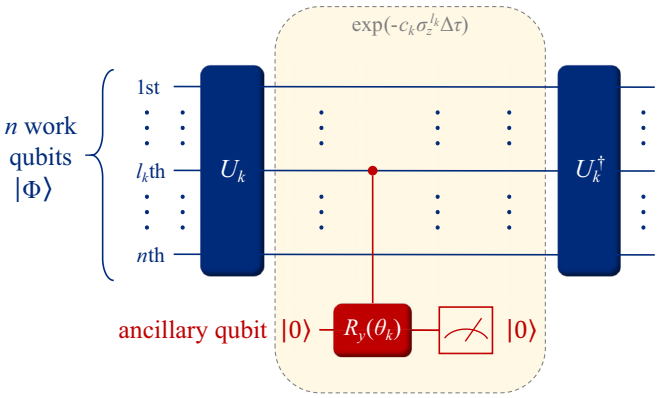

FIG. 1. Quantum circuit for implementing $\tilde{T}_k$.

which is a single-qubit operator. Thus, we have

$$\tilde{T}_k = U_k^\dagger \exp\big(-|c_k|\sigma_z^{l_k}\Delta\tau\big) U_k. \tag{4}$$

In Fig. 1 we present how to implement $\tilde{T}_k$ in a quantum circuit. The construction of U_k requires at most $O(n)$ single-qubit gates and controlled-NOT (CNOT) gates (see Appendix B for details).

After the action of U_k, we express the work-qubit state as $U_k |\Phi\rangle = a_0 |\psi_0\rangle + a_1 |\psi_1\rangle$, where $|\psi_0\rangle$ and $|\psi_1\rangle$ are the projection of $U_k |\Phi\rangle$ on the subspace where the l_kth qubit is $|0\rangle$ and $|1\rangle$, respectively. In Appendix B we demonstrate that a_0 and a_1 are also the amplitudes of the projection of $|\Phi\rangle$ on the ground-state subspace and excited-state subspace of $c_k h_k$, respectively. To implement $e^{-|c_k|\sigma_z\Delta\tau}$ on the l_kth work qubit, we add an ancillary qubit $|0\rangle$ and apply the controlled-R_y operation $|0\rangle\langle 0| \otimes I + |1\rangle\langle 1| \otimes R_y(\theta_k)$ on the l_kth work qubit and the ancillary qubit, where

$$\begin{aligned} R_y(\theta) &= e^{-i\theta\sigma_y/2} = \begin{pmatrix} \cos\theta/2 & -\sin\theta/2 \\ \sin\theta/2 & \cos\theta/2 \end{pmatrix}, \\ \theta_k &= 2\cos^{-1}(e^{-2|c_k|\Delta\tau}), \\ R_y(\theta_k) &= \begin{pmatrix} e^{-2|c_k|\Delta\tau} & -\sqrt{1-e^{-4|c_k|\Delta\tau}} \\ \sqrt{1-e^{-4|c_k|\Delta\tau}} & e^{-2|c_k|\Delta\tau} \end{pmatrix}, \end{aligned} \tag{5}$$

which gives the state

$$\begin{aligned} &a_0 |\psi_0\rangle |0\rangle_{\text{anc}} + a_1 e^{-2|c_k|\Delta\tau} |\psi_1\rangle |0\rangle_{\text{anc}} \\ &\quad + a_1\sqrt{1-e^{-4|c_k|\Delta\tau}} |\psi_1\rangle |1\rangle_{\text{anc}}. \end{aligned} \tag{6}$$

Then we measure the ancillary qubit, and if the result is 0, we obtain

$$\sqrt{\frac{1}{|a_0|^2 + |a_1|^2 e^{-4|c_k|\Delta\tau}}} (a_0 |\psi_0\rangle + a_1 e^{-2|c_k|\Delta\tau} |\psi_1\rangle), \tag{7}$$

which is equivalent to the result of $e^{-|c_k|\sigma_z\Delta\tau}$ acting on the l_kth work qubit up to normalization.

The probability of obtaining 0 in the measurement of the ancillary qubit is $|a_0|^2 + |a_1|^2 e^{-4|c_k|\Delta\tau}$. If we obtain 0, then the last step is to apply $U_k^\dagger$ on the work qubits. The output state will be exactly $\tilde{T}_k |\Phi\rangle$ up to normalization.

In summary, the nonunitary operator $\tilde{T}_k$ acting on a quantum state $|\Phi\rangle$ can be written as

$$\tilde{T}_k |\Phi\rangle = U_k^\dagger (\langle 0|_{\text{anc}} \mathcal{R}_k U_k |\Phi\rangle \otimes |0\rangle_{\text{anc}}), \tag{8}$$

up to a constant coefficient, where U_k transforms h_k into a Pauli matrix acting on the l_kth work qubit and $\mathcal{R}_k$ represents the controlled-R_y gate acting on the l_kth work qubit and the ancillary qubit, with rotation angle $\theta_k = 2\cos^{-1}(e^{-2|c_k|\Delta\tau})$.

III. RESULTS

To illustrate the performance of the PITE algorithm, we apply it to calculate the ground-state energy of three physical systems: H_2 molecules, LiH molecules, and a quantum Ising spin chain with both transverse and longitudinal fields. The calculations of H_2 are performed on Quafu's ten-qubit superconducting quantum processor and IonQ's eleven-qubit trapped-ion quantum processor. The calculations of LiH and the Ising chain are performed on a numerical simulator to study the influence of noise and the success probability of the algorithm.

A. Calculating the ground state of H_2 on quantum devices

To calculate the ground state of H_2 on a quantum computer, we first encode the molecular Hamiltonian into qubits. Here we choose the STO-3G basis [49] and use the Jordan-Wigner transformation (see Appendix D for details). We eventually obtain Hamiltonians composed of Pauli matrices $\mathcal{H}(R) = \sum_k c_k(R)\sigma_{\alpha_1}^1 \cdots \sigma_{\alpha_n}^n$, which act on n qubits. The coefficients c_k in each term vary with the interatomic distance R. The Hamiltonian of H_2 and LiH can be encoded onto four and six qubits, respectively. Further mapping is applied on H_2 to compactly encode the H_2 Hamiltonian into two qubits (see Ref. [50] for details), which gives the H_2 Hamiltonian in the form

$$\begin{aligned}\mathcal{H}_{H_2} = {} & c_0(R) + c_1(R)\sigma_z^1 + c_1(R)\sigma_z^2 \\ & + c_2(R)\sigma_z^1\sigma_z^2 + c_3(R)\sigma_x^1\sigma_x^2,\end{aligned} \tag{9}$$

where the coefficients at different R are available in Appendix D. The Hamiltonian for LiH at its lowest-energy interatomic distance (bond distance) is given explicitly in Appendix D.

In the demonstration on the quantum cloud platform, we use two qubits as the work qubits to represent the H_2 molecule and one qubit as the ancillary qubit. The Hartree-Fock state of H_2 is $|\Phi_{\text{HF}}\rangle = |00\rangle$ in the qubit representation, which is chosen as the initial state of the work qubits. Following the PITE method, we first perform the calculation at a fixed interatomic distance $R = 0.75$ Å and the algorithm is performed on Quafu's superconducting QPU P-10 and IonQ's trapped-ion QPU (for information of Quafu, see Appendix A). After each Trotter step, we tomograph the quantum state of the work qubits, with 2000 shots on Quafu and 1000 shots on IonQ. Then the state is used to calculate the energy value and is set as the initial state for the next step. The quantum circuits and related details are provided in Appendix E. The results of the energy expectation value as a function of the imaginary time

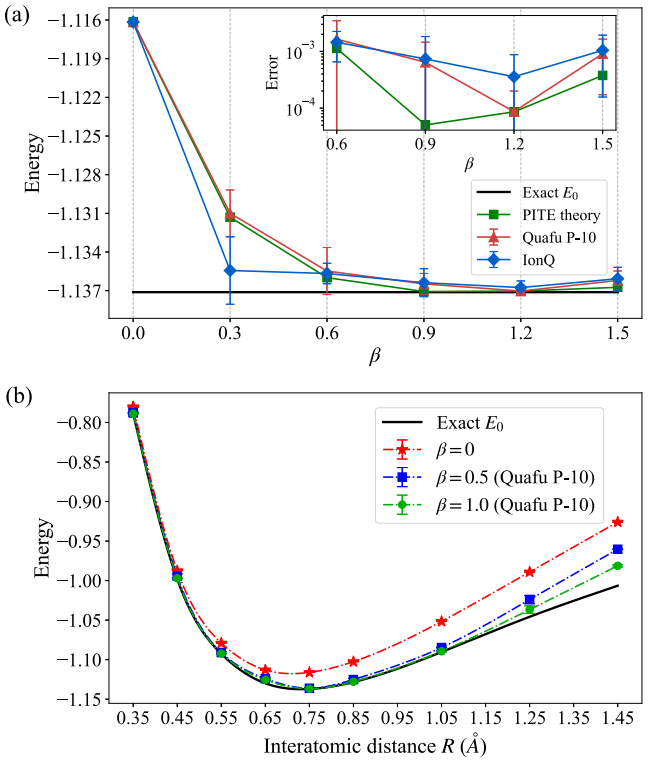

FIG. 2. Results of calculating the ground-state energy of H_2 on the Quafu and IonQ cloud platforms. (a) Energy values $E = \langle\Phi|\mathcal{H}_{H_2}|\Phi\rangle$ as a function of the imaginary time β at a fixed interatomic distance $R = 0.75$ Å. (b) Energy values $E = \langle\Phi|\mathcal{H}_{H_2}|\Phi\rangle$ as a function of β and the interatomic distance R. The black lines in (a) and (b) represent the exact ground-state energies obtained by diagonalization. The identity terms in the Hamiltonians are considered when calculating the energy values but not considered when executing the algorithm.

β are presented in Fig. 2(a) compared with the theoretical PITE results. As β increases, the energy rapidly converges to the exact solution E_0 in five evolution steps within an error of approximately 10^{-4} a.u, which is within the chemical precision.

To obtain the most stable molecular structure, we vary the interatomic distance and plot the potential-energy surfaces for the H_2 molecule, as shown in Fig. 2(b). These tasks are conducted only on Quafu's P-10, and the results ($\beta = 0.5$ and 1) are compared with the Hartree-Fock state energies ($\beta = 0$) and the exact ground-state energies obtained by diagonalization. The lowest energy in the potential-energy surface corresponds to the bound distance of the H_2 molecule, which is approximately 0.75 Å.

B. Numerical simulations of LiH and the quantum Ising chain

In the numerical simulations, we calculate the ground-state energies of LiH and the quantum Ising chain to study the success probability and the influence of noise. For LiH, we use six work qubits and one ancillary qubit. The Hartree-Fock state is $|\Phi_{\text{HF}}\rangle = |110000\rangle$ in the qubit representation. Here $|\Phi_{\text{HF}}\rangle$ is very close to the exact ground state; thus, it takes few steps for the state to converge. Therefore, to illustrate the convergence

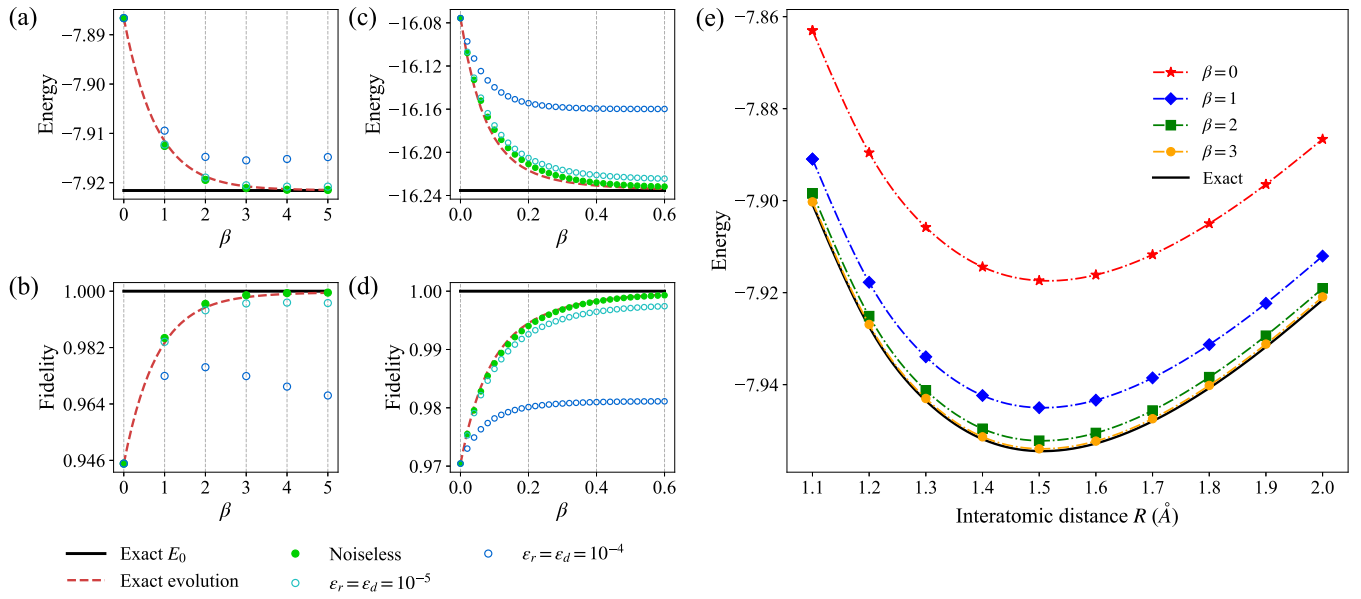

FIG. 3. Numerical simulation results of LiH and quantum Ising chain obtained from the PITE algorithm. (a) Energy values of LiH as a function of β. (b) Fidelity values of LiH as a function of β. The results in (a) and (b) are obtained at a fixed interatomic distance $R = 2.0$ Å. (c) Energy values of the Ising chain as a function of β. (d) Fidelity values of the Ising chain as a function of β. (e) Energy values of LiH as a function of β and the interatomic distance R. For LiH, the identity term in the Hamiltonian is considered when calculating the energy values but not considered when executing the algorithm. For the Ising chain, the parameters are chosen as $n = 10$, $J = 1$, $g = 1.2$, and $h = 0.3$. The black lines in (a), (c), and (e) represent the exact ground-state energies obtained by diagonalization. The red dashed lines in [(a)–(d)] are results of exact imaginary-time evolution.

process in greater detail, we use a superposition of $|\Phi_{\mathrm{HF}}\rangle$ and an excited state, $|\Phi_0\rangle = \sqrt{0.96}\,|\Phi_{\mathrm{HF}}\rangle + 0.2\,|000011\rangle$, as the initial state. Figures 3(a) and 3(b) display the convergence of the energy $E(\beta)$ and the fidelity $\mathcal{F}(\beta)$ as a function of β, respectively, where $\mathcal{F}(\beta) = |\langle E_0|\Phi_\beta\rangle|^2$ is the fidelity between $|\Phi_\beta\rangle$ and the exact ground state $|E_0\rangle$. The results are compared with the exact evolution (red dashed lines). The influence of quantum noise is studied by applying quantum channels on all qubits before each measurement of the ancillary qubit. The noise is described by

$$\mathcal{E}(\rho) = \sum_{\nu=1}^{3} \hat{E}_\nu \rho \hat{E}_\nu^\dagger, \tag{10}$$

with Kraus operators

$$\hat{E}_1 = \begin{pmatrix} 1 & 0 \\ 0 & \sqrt{1-\epsilon_{\mathrm{r}}-\epsilon_{\mathrm{d}}} \end{pmatrix},$$
$$\hat{E}_2 = \begin{pmatrix} 0 & \sqrt{\epsilon_{\mathrm{d}}} \\ 0 & 0 \end{pmatrix}, \quad \hat{E}_3 = \begin{pmatrix} 0 & 0 \\ 0 & \sqrt{\epsilon_{\mathrm{r}}} \end{pmatrix}, \tag{11}$$

where ϵ_{r} and ϵ_{d} are the relaxation parameter and dephasing parameter, respectively (see Appendix G for details). The simulation results are also presented in Figs. 3(a) and 3(b), which indicate the energy still converges to the exact solution within an error of approximately 10^{-3} a.u. under noisy conditions.

We vary the interatomic distance and plot the potential-energy surfaces for the LiH molecule, as shown in Fig. 3(e). The simulation results at different β and the exact solutions obtained by diagonalization are compared. The lowest energy in the potential-energy surface corresponds to the bound distance of the LiH molecule, which is approximately 1.5 Å.

Finally, we compute the ground-state energy of an n-site cyclic quantum Ising chain with the Hamiltonian

$$\mathcal{H} = -J \sum_{j=1}^{n} \left(\sigma_z^j \sigma_z^{j+1} + g\sigma_x^j + h\sigma_z^j\right), \quad \sigma_z^{n+1} = \sigma_z^1, \tag{12}$$

where g and h are the magnitudes of the transverse and longitudinal fields, respectively. In the simulation, the state of the work qubits is initialized as $|\Phi_0\rangle = (\cos\frac{\phi_0}{2}\,|0\rangle + \sin\frac{\phi_0}{2}\,|1\rangle)^{\otimes n}$, where ϕ_0 is chosen to minimize the initial energy $E(\beta = 0) = \langle\Phi_0|\mathcal{H}|\Phi_0\rangle$. In Figs. 3(c) and 3(d) we show the energy and fidelity values obtained by the PITE algorithm, as well as the influences of noises. The results show that the energy converges to the exact value within an error of approximately 10^{-3} in the noiseless case and approximately 10^{-2} in the noisy case.

C. Computational complexity

For one successfully executed quantum circuit, the number of quantum gates is $O(nmL)$, where n is the number of qubits, m is the number of terms in the Hamiltonian, and $L = \beta/\Delta\tau$ is the number of iteration steps. The depth of the quantum circuit is $O(mL)$. The main aspect of computational complexity we consider is the probability P of successfully generating $|\Phi_\beta\rangle$ due to the probabilistic measurements. In other words, $1/P$ is the average time to successfully generate $|\Phi_\beta\rangle$ through repeating the algorithm with majority-vote techniques.

For a quantum circuit that implements $\tilde{T}_k$, the probability of obtaining $|0\rangle$ from the ancillary qubit, according to Eq. (6), is

$$P_k = |a_0|^2 + |a_1|^2 e^{-4|c_k|\Delta\tau} \geqslant e^{-4|c_k|\Delta\tau}, \tag{13}$$

where $|a_0|^2 + |a_1|^2 = 1$. Thus, we have a rigorous lower bound (RLB) of the final success probability as a function of the imaginary time β,

$$\begin{aligned} P_{\text{final}} &\geqslant \left(\prod_{k=1}^{m} e^{-4|c_k|\Delta\tau}\right)^{\beta/\Delta\tau} \\ &= \exp\left(-4\beta \sum_k |c_k|\right) = P_{\text{RLB}}, \end{aligned} \tag{14}$$

which is exponential to β and the sum of $|c_k|'$s. It should be noted that the RLB is reached if and only if $a_0 = 0$ in Eq. (13) for all Pauli terms during the entire evolution process, which is the worst case and never occurs. In practice, a much greater success probability than the RLB can be reached (we will show the results in Sec. III B). A more practical lower bound [approximate lower bound (ALB)] of success probability is estimated. With $\langle\Phi|c_k h_k|\Phi\rangle = |c_k|(|a_1|^2 - |a_0|^2) = |c_k|(1 - 2|a_1|^2)$, we have the approximation

$$\begin{aligned} P_k &\approx |a_0|^2 + |a_1|^2(1 - 4|c_k|\Delta\tau) \\ &= 1 - 4|a_1|^2|c_k|\Delta\tau \\ &= 1 - 2\Delta\tau(\langle\Phi|c_k h_k|\Phi\rangle + |c_k|) \\ &\approx \exp[-2\Delta\tau(\langle\Phi|c_k h_k|\Phi\rangle + |c_k|)], \end{aligned} \tag{15}$$

and the total success probability after $\Delta\tau$ is approximated by

$$\begin{aligned} P(\Delta\tau) &\approx \prod_{k=1}^{m} P_k \\ &= \exp\left[-2\Delta\tau\left(\langle\Phi|\mathcal{H}|\Phi\rangle + \sum_k |c_k|^2\right)\right]. \end{aligned} \tag{16}$$

Here we are approximating that $|\Phi\rangle$ is constant during $\Delta\tau$. Thus the final success probability after imaginary time β is

$$P_{\text{final}} \approx \exp\left[-2\int_0^\beta d\tau\left(\langle\Phi|\mathcal{H}|\Phi\rangle + \sum_k |c_k|^2\right)\right]. \tag{17}$$

To do this integral, we need to evaluate the energy expectation value as a function of τ. We start with the initial normalized quantum state $|\Phi_0\rangle$, which is a linear combination of all eigenstates of the Hamiltonian:

$$|\Phi_0\rangle = \sum_{i=0} \mu_i |E_i\rangle . \tag{18}$$

Suppose the eigenvalues E_i are ordered as $E_0 \leqslant E_1 \leqslant E_2 \leqslant \cdots$. The normalized evolving state at imaginary time τ is

$$|\Phi_\tau\rangle = \frac{\sum_{i=0} \mu_i e^{-E_i\tau}|E_i\rangle}{\sqrt{\sum_{i=0} |\mu_i|^2 e^{-2E_i\tau}}}, \tag{19}$$

and the energy expectation value at imaginary time τ is

$$\begin{aligned} \langle\Phi_\tau|\mathcal{H}|\Phi_\tau\rangle &= \frac{\sum_{i=0} E_i|\mu_i e^{-E_i\tau}|^2}{\sum_{i=0} |\mu_i|^2 e^{-2E_i\tau}} \\ &= \frac{\sum_{i=0} s_i E_i e^{-2E_i\tau}}{\sum_{i=0} s_i e^{-2E_i\tau}} \\ &= \frac{s_0 E_0 + \sum_{i=1} s_i E_i e^{-2\Omega_i\tau}}{s_0 + \sum_{i=1} s_i e^{-2\Omega_i\tau}} \\ &= E_0 + \frac{\sum_{i=1} s_i \Omega_i e^{-2\Omega_i\tau}}{s_0 + \sum_{i=1} s_i e^{-2\Omega_i\tau}} \\ &\leqslant E_0 + \frac{(1 - s_0)\Omega_{\max} e^{-2\Omega_1\tau}}{s_0}, \end{aligned} \tag{20}$$

where $s_i = |\mu_i|^2$, $\Omega_i = E_i - E_0$, $\Omega_{\max}$ is the maximum of the Ω_i's, E_0 is the exact ground-state energy, and $s_0 = |\langle E_0|\Phi_0\rangle|^2$ is the fidelity between the initial state $|\Phi_0\rangle$ and the exact ground state $|E_0\rangle$. Returning to Eq. (17), we have the lower bound (ALB) of the final success probability as

$$\begin{aligned} P_{\text{final}} &\geqslant P_{\text{ALB}} \\ &= \exp\left(-2\beta\eta - \frac{(1 - s_0)\Omega_{\max}}{s_0\Omega_1}(1 - e^{-2\beta\Omega_1})\right), \end{aligned} \tag{21}$$

where $\eta = E_0 + \sum_k |c_k|$, which depends on the Hamiltonian spectrum.

One of the applications of imaginary-time evolution is to find the ground state and the corresponding eigenvalue, which is of broad interest in quantum computation science [43,51–53]. In this kind of problem we focus merely on the relation between the success probability and output error. The output error is defined as $\epsilon = 1 - \mathcal{F}$, where $\mathcal{F} = |\langle E_0|\Phi\rangle|^2$ is the fidelity. From Eq. (19) we have

$$\begin{aligned} \mathcal{F}(\beta) = |\langle E_0|\Phi_\beta\rangle|^2 &= \left|\frac{\sum_{i=0} \langle E_0|\mu_i e^{-\beta E_i}|E_i\rangle}{\sqrt{\sum_{i=0} |\mu_i|^2 e^{-2\beta E_i}}}\right|^2 \\ &= \frac{|\mu_0|^2 e^{-2\beta E_0}}{\sum_{i=0} |\mu_i|^2 e^{-2\beta E_i}} \\ &= \frac{s_0}{s_0 + \sum_{i=1} s_i e^{-2\beta\Omega_i}} \\ &\geqslant \frac{s_0}{s_0 + (1 - s_0)e^{-2\beta\Omega_1}}, \end{aligned} \tag{22}$$

where we could use $1 - s_0 = \sum_{i=1} s_i$ and $\Omega_i \geqslant \Omega_1$ for all i's. This leads to

$$\beta\Omega_1 \leqslant \frac{1}{2}\ln\left(\frac{1 - s_0}{s_0}\frac{1 - \epsilon}{\epsilon}\right). \tag{23}$$

Here we write the product of β and Ω_1 because we can choose the scale of the Hamiltonian to change the value of Ω_1, and β is also dependent on the scale of the Hamiltonian. So it is the product $\beta\Omega_1$ that really matters. Equation (23) indicates that

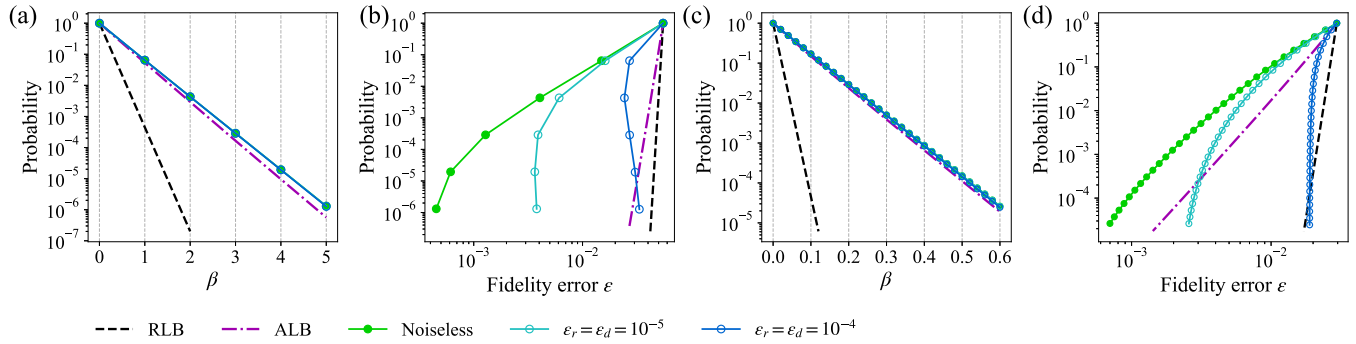

FIG. 4. Success probabilities of PITE in numerical simulations of LiH molecules and the quantum Ising chain. (a) Success probability of LiH as a function of the imaginary time β. (b) Success probability of LiH as a function of the output fidelity error ϵ. (c) Success probability of the Ising chain as a function of β. (d) Success probability of the Ising chain as a function of the output fidelity error ϵ. In (b) and (d) the initial states are at the top right side of the figures and evolve toward the bottom left side. For LiH, the RLBs and ALBs are calculated without the identity term of the Hamiltonian.

the required imaginary-time length $\beta = O(\Omega_1^{-1} \log \epsilon^{-1})$ when the output error is lower than ϵ is logarithmically dependent on the inverse of ϵ and linearly dependent on the inverse of the energy gap of the Hamiltonian. Here we do not consider the error caused by Trotter decomposition (2), which may reduce the fidelity in Eq. (22) by $O(\Delta\tau)$. This error causes the quantum state to fail to reach the ground state with arbitrary precision and it cannot be reduced by increasing β. The quantum state would converge to $|E_0\rangle + |\delta\rangle$ as β increases, where $||\delta\rangle| \sim O(\Delta\tau)$. However, we can reduce the error term to $O(\Delta\tau^2)$ using the higher-order decomposition [54]

$$e^{-\beta\mathcal{H}} = [(e^{-c_1 h_1 \Delta\tau/2} \cdots e^{-c_M h_M \Delta\tau/2}) \times (e^{-c_M h_M \Delta\tau/2} \cdots e^{-c_1 h_1 \Delta\tau/2})]^{\beta/\Delta\tau} + O(\Delta\tau^2). \tag{24}$$

Connecting Eqs. (14), (21), and (23) shows the RLB and ALB of the final success probability when the output error is less than ϵ,

$$\begin{aligned} P_{\mathrm{RLB}} &\geqslant \left(\frac{s_0}{1-s_0}\frac{\epsilon}{1-\epsilon}\right)^{\kappa_0} = O(\epsilon^{\kappa_0}), \\ P_{\mathrm{ALB}} &\geqslant \left(\frac{s_0}{1-s_0}\frac{\epsilon}{1-\epsilon}\right)^{\kappa_1} \exp\left[-\frac{\Omega_{\max}}{s_0\Omega_1}\left(1-\frac{s_0}{1-\epsilon}\right)\right] \\ &= O(\epsilon^{\kappa_1}), \end{aligned} \tag{25}$$

where $\kappa_0 = 2\sum_k |c_k|/\Omega_1$ and $\kappa_1 = (E_0 + \sum_k |c_k|)/\Omega_1$ are dependent on the spectrum of the Hamiltonian but independent of the scale of the Hamiltonian.

All the lower bounds presented above remain unchanged when higher-order Trotter formulas are used. This is because the Trotter formula preserves the total accumulated time for each Hamiltonian term.

In Fig. 4 we present the success probabilities in the simulations of LiH and the Ising chain. The success probabilities as a function of β are shown in Figs. 4(a) and 4(c), which indicate exponential decay of the success probability as β increases. We can see that the ALB (purple dot-dashed lines) is a much better approximation to the simulation results than the RLB (black dashed lines) in both cases. The results indicate that the success probability is hardly affected by the noises. Figures 4(b) and 4(d) show the success probability as a function of the output error ϵ. We can see that the success probability can be lower than the ALB when qubits are affected by the noise.

IV. GENERALIZATION OF the PITE ALGORITHM

In this section we generalize the PITE algorithm for the Hamiltonian which is not expressed as a sum of Pauli terms. In general, the Hamiltonian is written as $\mathcal{H} = \sum_{k=1}^{m} H_k$ and the ITE operator is decomposed as

$$e^{-\beta\mathcal{H}} = (e^{-H_1\Delta\tau} \cdots e^{-H_m\Delta\tau})^{\beta/\Delta\tau} + O(\Delta\tau). \tag{26}$$

We assume that the eigenvalues of each term H_k can be efficiently obtained through classical calculation and that the corresponding eigenstates can be efficiently prepared on a quantum computer. This assumption is true for most cases, e.g., when H_k's are local operators. We denote by $\lambda_{k,i}$ the ith eigenvalue of H_k and by $|\lambda_{k,i}\rangle$ the corresponding eigenstate. We define $\omega_{k,i} = \lambda_{k,i} - \lambda_{k,0}$, where $\lambda_{k,0}$ is the lowest eigenvalue of H_k. The procedure of implementing the operator $e^{-H_k\Delta\tau}$ on a quantum computer is described as follows.

(i) Apply a unitary U_k to the work qubits, which transforms $|\lambda_{k,i}\rangle$ into computational basis $|x_{k,i}\rangle$.

(ii) Add an ancillary qubit which is initialized as $|0\rangle$.

(iii) Apply the gate $\sum_i |x_{k,i}\rangle\langle x_{k,i}| \otimes R_y(\theta_{k,i})$, where $\theta_{k,i} = 2\cos^{-1}(e^{-\omega_{k,i}\Delta\tau})$.

(iv) Measure the ancillary qubit. If 0 is obtained, continue the procedure; otherwise, start from the beginning.

(v) Apply $U_k^\dagger$ to the work qubits. End the procedure.

Note that it should be easy to implement U_k and $U_k^\dagger$ because we assume that $|\lambda_{k,i}\rangle'$s can be efficiently prepared on a quantum computer. Obviously, when H_k's are Pauli terms, this procedure degrades to the original version of the PITE algorithm; therefore, it is a GPITE algorithm.

Now we look into the complexity of GPITE. Similarly to the derivation in Sec. III C, it is not difficult to obtain the practical lower bound or ALB of the final success probability

$$P_{\mathrm{final}} \geqslant P_{\mathrm{ALB}} = \exp\left(-2\beta\eta' - \frac{(1-s_0)\Omega_{\max}}{s_0\Omega_1}(1-e^{-2\beta\Omega_1})\right), \tag{27}$$

where $\eta' = E_0 - \sum_k \lambda_{k,0}$ (see details in Appendix C). In particular, when $H_k = c_k h_k$ are Pauli terms, $\lambda_{k,0} = -|c_k|$, which turns Eq. (27) into Eq. (21).

According to Eq. (27), the GPITE can help us increase the success probability. When $\mathcal{H}$ is given, the only changeable part in Eq. (27) is $\sum_k \lambda_{k,0}$. This suggests that we can divide $\mathcal{H}$ into H_k's in different ways, which allows us to increase $\sum_k \lambda_{k,0}$ and improve the success probability.

Moreover, the circuit depth of GPITE depends linearly on the number of terms, which can be reduced by grouping fewer H_k's. Therefore, the GPITE improves the successful probability and reduces the gate complexity compared with the original version but requires more classical resources than diagonalizing H_k's. There exists a tradeoff and the crucial point is to find a good way to divide the terms of the Hamiltonian into proper groups according to the characteristics in the specific system.

We apply the GPITE in the simulations of LiH (at $R = 2.0$ Å) and the quantum Ising chain. Instead of taking $c_k h_k$ as H_k, we rearrange these terms and divide the Hamiltonian in another way (see Appendix F for details). The simulation results are presented in Fig. 5, where the success probabilities obtained by GPITE are compared with the generalized ALB given by Eq. (27) in Figs. 5(c) and 5(f). The results indicate that GPITE has little effect on reducing the output error, but the final success probabilities are increased by 10^2–10^4, which makes our algorithm much more practical.

We also run the simulation using the original PITE with second-order decomposition (24). As shown in Figs. 5(a)–5(f), the results of the second-order Trotter formula are closer to the exact evolution (red dashed lines).

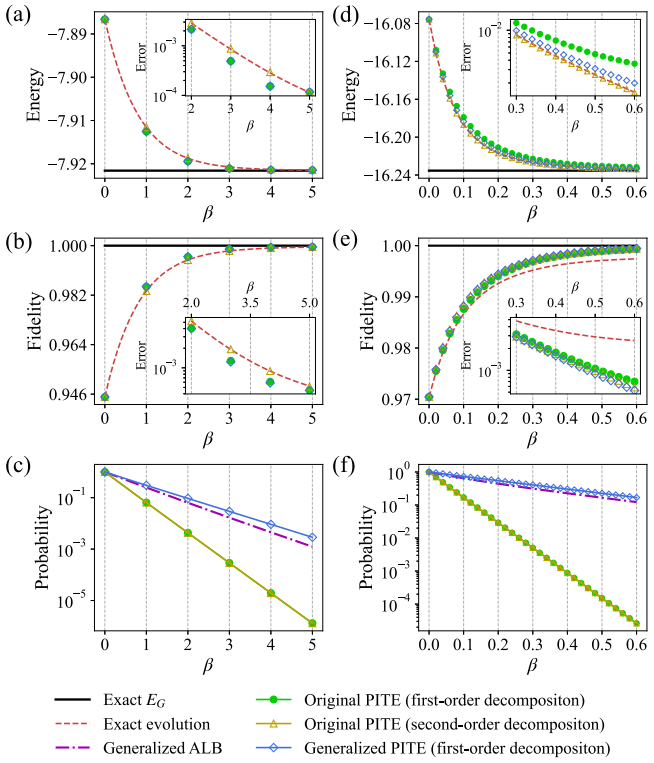

FIG. 5. Numerical simulation results of LiH molecules and the quantum Ising chain obtained from the generalized PITE algorithm. (a) Energy of LiH as a function of β. (b) Fidelity of LiH as a function of β. (c) Success probability of LiH as a function of β. (d) Energy of the Ising chain as a function of β. (e) Fidelity of the Ising chain as a function of β. (f) Success probability of the Ising chain as a function of β. The red dashed lines in (a), (b), (d), and (e) are results of exact imaginary-time evolution. For LiH, the interatomic distance is fixed as $R = 2.0$ Å and the identity term from the Hamiltonian is not considered when executing the algorithm or calculating the generalized ALB. For the Ising chain, the parameters are chosen as $n = 10$, $J = 1$, $g = 1.2$, and $h = 0.3$.

V. CONCLUSION

In this paper we proposed a probabilistic algorithm for implementing imaginary-time evolution, based on nonunitary quantum circuits, and presented the explicit construction of the circuit that is applicable to any number of qubits and any Hamiltonians that can be efficiently expressed as a sum of Pauli terms. This algorithm can be applied to solving the ground state of a Hamiltonian. For an n-qubit Hamiltonian composed of m Pauli terms, the algorithm returns the ground state within an error of ϵ with a success probability $P_{\text{final}} = O(\epsilon^{\kappa})$, where κ is determined by the spectrum of the Hamiltonian. The success probability decreases quickly as the energy gap between the ground and the first excited state of the Hamiltonian decreases. Generally speaking, most existing quantum algorithms are affected by the energy gap of the Hamiltonian. For example, a variational quantum eigensolver finds the minimum energy value using classical optimization methods, such as gradient descent. The energy gap influences the classical optimization, so the optimizing process could encounter the barren plateau problem [31]. For quantum phase estimation, the Harrow-Hassidim-Lloyd algorithm, and related algorithms, the energy gap is related to the condition number κ of the matrix and κ also influences the complexity of the algorithm. Classical algorithms, such as the matrix exponential $e^{-\beta H}$, consumes $O(N^3)$ [55] to achieve the same goal. As mentioned above, for one successfully executed quantum circuit, the gate complexity is $O(\log(N)mL)$. Therefore, for the whole algorithm, the space complexity is $O(\log N)$ and the time complexity is $O(\frac{\log(N)mL}{P_{\text{final}}})$. In the case that $P_{\text{final}} \geqslant 1/N^2$, our algorithm outperforms the corresponding classical algorithms.

We demonstrated the feasibility and performance of the proposed method with the example of H_2, LiH molecules, and the quantum Ising chain through quantum cloud platforms and numerical simulations. We also generalized this approach to the cases where the Hamiltonian is not composed of Pauli terms and illustrated its improvement on success probability in simulations.

Our algorithm goes beyond solving the ground-state energy and is specifically designed for implementing ITE. The success probability decays exponentially with β and the spectral radius of the Hamiltonian. This is a common problem in existing algorithms for ITE, because quantum algorithms employing nonunitary quantum circuits are inherently probabilistic [3,38,40]. However, we have made significant efforts to improve the success probability, such as proposing the GITE algorithm in Sec. IV. Beyond this article, another possible way to increase the success probability is to combine

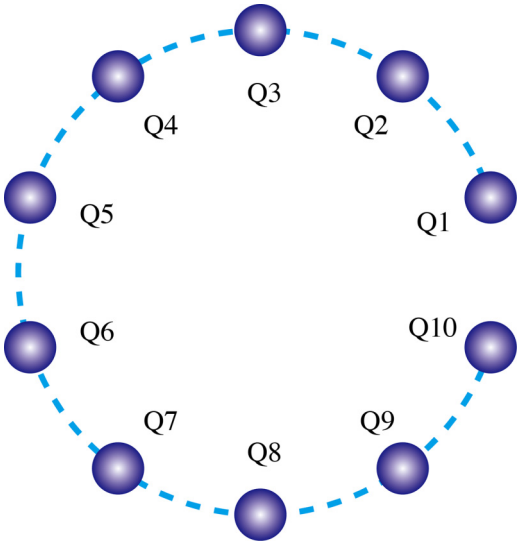

FIG. 6. Topological structure of quantum processor P-10. Each qubit is capacitively coupled to its nearest neighbors.

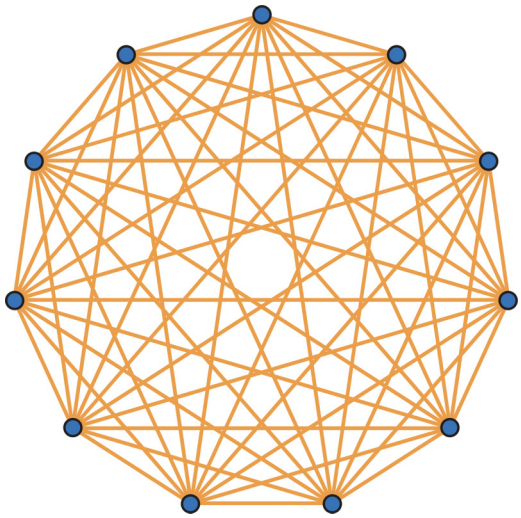

FIG. 7. Topological structure of the 11-qubit quantum processor of IonQ. All qubit are capacitively coupled to each other.

probabilistic methods and other methods, such as variational quantum algorithms, which is a topic left for future work. A similar work [56] describes PITE algorithm as a block encoding of the ITE operator. Given the ability to efficiently simulate ITE on quantum computers, one may explore the techniques for preparing thermal states or studying finite-temperature properties of quantum systems. Furthermore, the ITE algorithm can also be applied in non-Hermitian physics. By decomposing the Hamiltonian into its Hermitian and anti-Hermitian parts, we can apply the ITE algorithm to the evolution of the anti-Hermitian part, which allows us to simulate the dynamical process of a non-Hermitian Hamiltonian.

ACKNOWLEDGMENTS

This research was supported by National Basic Research Program of China. S.W. acknowledge the National Natural Science Foundation of China under Grants No. 12005015 and the Beijing Nova Program under Grants No. 20230484345. We gratefully acknowledge support from the Extreme Condition User Facility in Beijing, Quafu cloud platform for quantum computation, Beijing Advanced Innovation Center for Future Chip (ICFC).

APPENDIX A: QUAFU AND IONQ

Quafu is an open cloud platform for quantum computation [57]. It currently provides four specifications of superconducting quantum processors and three of them support general quantum logical gates, which are 10-qubit and 18-qubit processors with one-dimensional chain structures named P-10 and P-18, and a 50+-qubit processor with a two-dimensional honeycomb structure named P-50.

PyQuafu is an open-source software development kit for PYTHON based on the Quafu cloud platform. Users can easily install it through PYPI or source install with GitHub [58]. In this article we use the quantum processor of P-10, which is shown in Fig. 6. The processor consists of ten transmon qubits Q_1–Q_{10} arrayed in a row, with each qubit capacitively coupled to its nearest neighbors. Each transmon qubit can be modulated in frequency from about 4 to 5.7 GHz and excited to the excited state individually. All qubits can be probed through a common transmission line connected to their own readout resonators. The qubit parameters and coherence performance can be found in Table I. The idle frequencies of each qubit ω_j^{10} are designed to reduce residual coupling strength from other qubits.

IonQ is an open cloud platform for quantum computation [59] which currently provides an 11-qubit trapped-ion quantum processor. IonQ's QPUs are built on a chain of trapped $^{171}Yb^{+}$ ions, spatially confined via a microfabricated surface electrode trap within a vacuum chamber. The quantum processor used in this article is shown in Fig. 7, which shows an all-to-all connectivity of the trapped-ion qubits. The trapped ions are aligned to form a linear crystal, suspended in a chip trap with a radial pseudopotential frequency approximately equal to 3.1 MHz. The quantum gates are performed via a two-photon Raman transition using a pair of counterpropagating beams from a mode-locked pulsed laser. More information about the device can be found in Ref. [60].

APPENDIX B: UNITARY TRANSFORMATION OF PAULI PRODUCT TERMS

To realize $\tilde{T}_k = e^{-c_k h_k \Delta\tau}$ in quantum circuits, we apply a unitary transformation

$$U_k c_k h_k U_k^{\dagger} = -|c_k|\sigma_z^{l_k}, \quad l_k \in \{1, \ldots, n\}, \tag{B1}$$

which gives us

$$\tilde{T}_k = U_k^{\dagger} \exp\big(-|c_k|\sigma_z^{l_k}\Delta\tau\big)U_k. \tag{B2}$$

We will first prove that the unitary gate U_k which satisfies Eq. (B1), where $h_k = \sigma_{\alpha_1}^1 \otimes \cdots \otimes \sigma_{\alpha_n}^n$, can be constructed with $O(n)$ single-qubit CNOT gates. In fact, there are many methods to construct such a U_k. Here we will show one method, which is to decompose U_k into three unitaries: $U_k = V_3 V_2 V_1$.

TABLE I. Device parameters: ω_j^s shows the maximum frequency of Q_j; ω_j^{10} corresponds to the idle frequency of Q_j; ω_j^r shows the resonant frequency of Q_j during readout; η_j corresponds to the anharmonicity of Q_j; $g_{j,j+1}$ is the coupling strength between nearest-neighbor qubits; $T_{1,j}$ and $T_{2,j}^*$ represent the relaxation time and coherence time of Q_j, respectively; $F_{0,j}$ and $F_{1,j}$ are readout fidelities of Q_j in $|0\rangle$ and $|1\rangle$, respectively; and $F_{j,j+1}$ represents the fidelity of the CZ gate composed of Q_i and Q_j, which is obtained by randomized benchmarking.

Parameter \ Qubit	Q_1	Q_2	Q_3	Q_4	Q_5	Q_6	Q_7	Q_8	Q_9	Q_{10}
$\omega_j^s/2\pi$ (GHz)	5.536	5.069	5.660	4.742	5.528	4.929	5.451	4.920	5.540	4.960
$\omega_j^{10}/2\pi$ (GHz)	5.456	4.424	5.606	4.327	5.473	4.412	5.392	4.319	5.490	4.442
$\omega_j^r/2\pi$ (GHz)	5.088	4.702	5.606	4.466	5.300	4.804	5.177	4.697	5.474	4.819
$\eta_j/2\pi$ (GHz)	0.250	0.207	0.251	0.206	0.251	0.203	0.252	0.204	0.246	0.208
$g_{j,j+1}/2\pi$ (MHz)	12.07	11.58	10.92	10.84	11.56	10.00	11.74	11.70	11.69	
$T_{1,j}$ (μs)	20.0	52.5	15.9	16.3	36.9	44.4	30.8	77.7	22.8	25.0
$T_{2,j}^*$ (μs)	8.60	1.48	9.11	2.10	12.8	2.73	15.7	1.88	4.49	2.05
$F_{0,j}$ (%)	98.90	98.32	98.67	95.30	97.00	95.47	97.00	96.37	98.33	97.13
$F_{1,j}$ (%)	92.90	92.30	92.97	91.53	86.17	87.93	93.40	93.37	94.63	92.07
$F_{j,j+1}$ (%)	94.2	97.8	96.6	97.3	96.8	97.0	94.5	93.2	96.0	

Two examples of constructing U_k for five-qubit systems are shown in Fig. 8. First, we notice that

$$H\sigma_x H = \sigma_z, \quad HS^\dagger \sigma_y SH = \sigma_z, \tag{B3}$$

where H is the Hadamard gate and S is the $\pi/4$ phase gate, i.e., $S = e^{-i\pi\sigma_z/4}$. Thus, we construct V_1 by applying H and $HS^\dagger$ on those qubits whose corresponding Pauli matrices are σ_x and σ_y, respectively. Then we have

$$V_1 c_k \left(\sigma_{\alpha_1}^1 \otimes \cdots \otimes \sigma_{\alpha_n}^n\right) V_1^\dagger = c_k \sigma_{\gamma_1}^1 \otimes \cdots \otimes \sigma_{\gamma_n}^n, \tag{B4}$$

where $\gamma_j = 0$ if $\alpha_j = 0$ and $\gamma_j = z$ otherwise.

Next we note that

$$C_{i,j}\left(\sigma_z^i \otimes \sigma_z^j\right) C_{i,j} = I^i \otimes \sigma_z^j, \tag{B5}$$

where $C_{i,j}$ represents the CNOT gate with the ith qubit being the control qubit and the jth qubit being the target. To construct V_2, we first choose an arbitrary l with $\gamma_l = z$ and then apply $C_{j,l}$ for all j with $\gamma_j = z$ and $j \neq l$. Thus we have

$$V_2 V_1 c_k \left(\sigma_{\alpha_1}^1 \otimes \cdots \otimes \sigma_{\alpha_n}^n\right) V_1^\dagger V_2^\dagger = I^{\otimes l-1} \otimes c_k \sigma_z^l \otimes I^{\otimes n-l}. \tag{B6}$$

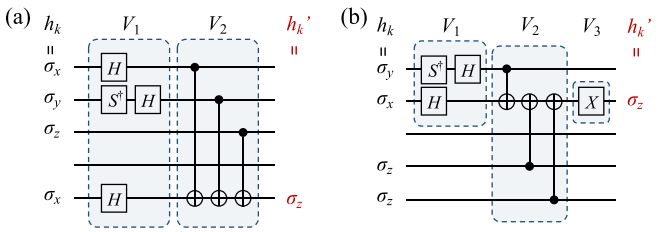

FIG. 8. Examples of the construction of U_k in five-qubit systems: (a) for $h_k = \sigma_x^1\sigma_y^2\sigma_z^3\sigma_x^5$, with $c_k < 0$, $U = V_2V_1$ and $Uc_kh_kU^\dagger = c_k\sigma_z^5$, and (b) for $h_k = \sigma_y^1\sigma_x^2\sigma_z^4\sigma_z^5$, with $c_k > 0$, $U = V_3V_2V_1$ and $Uc_kh_kU^\dagger = -c_k\sigma_z^2$. The V_1 transforms all Pauli operators into σ_z; V_2 transforms the product of σ_z's into a single qubit σ_z; and V_3, if it is not identity, puts a minus sign on σ_z.

For the last step, we have

$$\sigma_x\sigma_z\sigma_x = -\sigma_z. \tag{B7}$$

Therefore, if $c_k > 0$, $V_3 = \sigma_x^l$; otherwise $V_3 = I$.

By now, we have successfully constructed the unitary gate U_k which satisfied Eq. (B1) by $U_k = V_3V_2V_1$, and the maximum number of CNOT and single-qubit gates used in this procedure is $2n + (n-1) + 1 = 3n$, where n is the number of the qubit.

After the action of U_k, we write the state of work qubits as $U_k|\Phi\rangle = a_0|\psi_0\rangle + a_1|\psi_1\rangle$, where $|\psi_0\rangle$ and $|\psi_1\rangle$ are the projections of the work-qubit state on the subspace where the l_kth qubit is $|0\rangle$ and $|1\rangle$, respectively. Therefore,

$$|\Phi\rangle = a_0U_k^\dagger|\psi_0\rangle + a_1U_k^\dagger|\psi_1\rangle. \tag{B8}$$

From Eq. (B1) we have

$$c_kh_kU_k^\dagger|\psi_0\rangle = -|c_k|U_k^\dagger\sigma_z^{l_k}|\psi_0\rangle = -|c_k|U_k^\dagger|\psi_0\rangle, \tag{B9}$$

which indicates $U_k^\dagger|\psi_0\rangle$ is an eigenstate of c_kh_k with eigenvalue $-|c_k|$. Similarly, we can show that $U_k^\dagger|\psi_1\rangle$ is an eigenstate of c_kh_k with eigenvalue $|c_k|$. Therefore, from Eq. (B8) we can say that a_0 and a_1 are the amplitudes of the projection of $|\Phi\rangle$ on the ground-state subspace and excited-state subspace of c_kh_k, respectively.

APPENDIX C: COMPLEXITY OF GPITE

For GPITE, the derivation of the complexity is similar to the derivation in Sec. III C. The probability of successfully implementing $e^{-H_k\Delta\tau}$, if following the procedure described in Sec. IV, is

$$P_k(\Delta\tau) = |a_0|^2 + \sum_{i=1} |a_i|^2 e^{-2\omega_{k,i}\Delta\tau}, \tag{C1}$$

where $a_i = \langle\lambda_{k,i}|\Phi\rangle$ $(i \geqslant 0)$ and $\omega_{k,i} = \lambda_{k,i} - \lambda_{k,0}$ ($\lambda_{k,0}$ is the lowest eigenvalue of H_k). Take the approximation of

Eq. (C1) as

$$\begin{aligned} P_k(\Delta\tau) &\approx |a_0|^2 + \sum_{i=1} |a_i|^2(1-2\omega_{k,i}\Delta\tau) \\ &= 1 - 2\Delta\tau \sum_{i=1} |a_i|^2 \omega_{k,i} \\ &= 1 - 2\Delta\tau(\langle\Phi_\tau|H_k|\Phi_\tau\rangle - \lambda_{k,0}) \\ &\approx \exp[-2\Delta\tau(\langle\Phi_\tau|H_k|\Phi_\tau\rangle - \lambda_{k,0})], \end{aligned} \tag{C2}$$

and the total success probability after $\Delta\tau$ is approximated by

$$\begin{aligned} P(\Delta\tau) &\approx \prod_{k=1}^{m} P_k(\Delta\tau) \\ &= \exp\left[-2\Delta\tau\left(\langle\Phi_\tau|\mathcal{H}|\Phi_\tau\rangle - \sum_k \lambda_{k,0}\right)\right]. \end{aligned} \tag{C3}$$

Here we are approximating that $|\Phi\rangle$ is constant during $\Delta\tau$. Thus the final success probability after imaginary time β is

$$\begin{aligned} P_{\text{final}} &\approx \exp\left[-2\int_0^\beta \mathrm{d}\tau\left(\langle\Phi_\tau|\mathcal{H}|\Phi_\tau\rangle - \sum_k \lambda_{k,0}\right)\right] \\ &\geqslant \exp\left[-2\beta\left(E_0 - \sum_k \lambda_{k,0}\right)\right. \\ &\quad \left. - \frac{(1-s_0)\Omega_{\max}}{s_0\Omega_1}(1-e^{-2\beta\Omega_1})\right], \end{aligned} \tag{C4}$$

where we use Eq. (20) to do the integral. This result gives us the lower bound (ALB) of the final success probability. In particular, when $H_k = c_k h_k$ are Pauli terms, $\lambda_{k,0} = -|c_k|$, which turns Eq. (C4) into Eq. (21). We note that when $\mathcal{H}$ is given, the only changeable part in Eq. (27) is $\sum_k \lambda_{k,0}$. By increasing this part we can enlarge the success probability.

Furthermore, when using imaginary-time evolution to determine the ground state, we actually care about the probability as a function of the error $\epsilon = 1 - \mathcal{F}$ instead of β. Therefore, we connect Eqs. (23) and (C4) and obtain the relation between the success probability and the output error

$$\begin{aligned} P_{\text{ALB}} &\geqslant \left(\frac{s_0}{1-s_0}\frac{\epsilon}{1-\epsilon}\right)^\kappa \exp\left[-\frac{\Omega_{\max}}{s_0\Omega_1}\left(1-\frac{s_0}{1-\epsilon}\right)\right] \\ &= O(\epsilon^\kappa), \end{aligned} \tag{C5}$$

where $\kappa = (E_0 - \sum_k \lambda_{k,0})/\Omega_1$ is independent of the scale of Hamiltonian. This indicates that if we hope to obtain the ground state within an error of ϵ, the success probability is supposed to be $P = O(\epsilon^\kappa)$ and we have to repeat the algorithm $1/P$ times on average to get the desired state.

APPENDIX D: MAPPING THE HAMILTONIAN OF H_2 AND LiH TO QUBITS

A molecule is a many-body system composed of nuclei and electrons. Its Hamiltonian includes the kinetic energy of each particle and the Coulomb potential energy between any two of these particles, written as

$$\begin{aligned} \mathcal{H} = &-\sum_i \frac{1}{2M_i}\nabla_{R_i}^2 - \sum_i \frac{1}{2}\nabla_{r_i}^2 - \sum_{i,j}\frac{Z_j}{|r_i - R_j|^2} \\ &+ \sum_{i,j}\frac{Z_i Z_j}{|R_i - R_j|^2} + \sum_{i,j}\frac{1}{|r_i - r_j|^2}, \end{aligned} \tag{D1}$$

in atomic units, where M_i, Z_i, R_i, and r_i are the masses, charges, positions of nuclei, and positions of electrons, respectively. We first apply the Born-Oppenheimer approximation, which assumes the nuclear coordinates are parameters rather than variables. Then the Hamiltonian is projected onto a chosen set of orbitals. Here we choose the standard Gaussian STO-3G basis [49] and rewrite the Hamiltonian in the second-quantized form

$$\mathcal{H} = \sum_{ij} u_{ij} a_i^\dagger a_j + \sum_{ijkl} u_{ijkl} a_i^\dagger a_j^\dagger a_k a_l + \cdots, \tag{D2}$$

where $a_i^\dagger$ and a_j are the creation and annihilation operators of particle in the ith and jth orbitals, respectively, and the ellipsis represents the high-order interactions.

To map the fermionic Hamiltonian to the qubit Hamiltonian, we use the Jordan-Wigner transformation (JWT), which could transform the creation and annihilation operators into Pauli matrices. Under the JWT, the state of the jth qubit $|0\rangle$ or $|1\rangle$ corresponds to the jth orbital being unoccupied or occupied, respectively.

For H_2 molecules, we use the method described in Supplemental Material of Ref. [50] to get the qubit Hamiltonian with two qubits, which is written as

$$\mathcal{H}_{H_2} = c_0 + c_1\sigma_z^1 + c_1\sigma_z^2 + c_2\sigma_z^1\sigma_z^2 + c_3\sigma_x^1\sigma_x^2. \tag{D3}$$

The exact coefficients used in our work are shown in Table II.

TABLE II. Coefficients in the H_2 Hamiltonian at different interatomic distances R.

R (Å)	c_0	c_1	c_2	c_3
0.35	7.01273×10^{-1}	-7.47416×10^{-1}	1.31036×10^{-2}	1.62573×10^{-1}
0.45	2.67547×10^{-1}	-6.33890×10^{-1}	1.27192×10^{-2}	1.66621×10^{-1}
0.55	-1.83734×10^{-2}	-5.36489×10^{-1}	1.23003×10^{-2}	1.71244×10^{-1}
0.65	-2.13932×10^{-1}	-4.55433×10^{-1}	1.18019×10^{-2}	1.76318×10^{-1}
0.75	-3.49833×10^{-1}	-3.88748×10^{-1}	1.11772×10^{-2}	1.81771×10^{-1}
0.85	-4.45424×10^{-1}	-3.33747×10^{-1}	1.04061×10^{-2}	1.87562×10^{-1}
1.05	-5.62600×10^{-1}	-2.48783×10^{-1}	8.50998×10^{-3}	1.99984×10^{-1}
1.25	-6.23223×10^{-1}	-1.86173×10^{-1}	6.45563×10^{-3}	2.13102×10^{-1}
1.45	-6.52661×10^{-1}	-1.38977×10^{-1}	4.59760×10^{-3}	2.26294×10^{-1}

TABLE III. The LiH Hamiltonian at bound distance, as well as the grouping of the Pauli terms used in generalized PITE.

k	c_k	h_k	$H_{k'}$	k	c_k	h_k	$H_{k'}$
1	-7.35094	$\mathbf{1}$		33	-1.49854×10^{-3}	$\sigma_x^2\sigma_z^3\sigma_x^4\sigma_z^5$	H_{13}
2	-1.58950×10^{-1}	σ_z^1	H_1	34	-1.49854×10^{-2}	$\sigma_y^2\sigma_z^3\sigma_y^4\sigma_z^5$	H_{13}
3	-1.58950×10^{-1}	σ_z^2	H_1	35	1.13678×10^{-2}	$\sigma_x^1\sigma_z^2\sigma_z^3\sigma_x^6$	H_{14}
4	7.82811×10^{-2}	$\sigma_z^1\sigma_z^2$	H_1	36	1.13678×10^{-2}	$\sigma_y^1\sigma_z^2\sigma_z^3\sigma_y^6$	H_{14}
5	-1.45795×10^{-1}	σ_z^3	H_2	37	-1.17598×10^{-3}	$\sigma_z^1\sigma_x^2\sigma_z^3\sigma_x^4$	H_{15}
6	-1.45795×10^{-1}	σ_z^4	H_2	38	-1.17598×10^{-3}	$\sigma_z^1\sigma_y^2\sigma_z^3\sigma_y^4$	H_{15}
7	8.51132×10^{-2}	$\sigma_z^3\sigma_z^4$	H_2	39	3.56300×10^{-3}	$\sigma_x^1\sigma_z^2\sigma_x^3\sigma_z^5$	H_{16}
8	2.96723×10^{-2}	σ_z^5	H_3	40	3.56300×10^{-3}	$\sigma_y^1\sigma_z^2\sigma_y^3\sigma_z^5$	H_{16}
9	2.96723×10^{-2}	σ_z^6	H_3	41	3.56300×10^{-3}	$\sigma_x^2\sigma_z^3\sigma_x^4\sigma_z^6$	H_{17}
10	1.24302×10^{-1}	$\sigma_z^5\sigma_z^6$	H_3	42	3.56300×10^{-3}	$\sigma_y^2\sigma_z^3\sigma_y^4\sigma_z^6$	H_{17}
11	5.36162×10^{-2}	$\sigma_z^1\sigma_z^3$	H_4	43	-1.03458×10^{-2}	$\sigma_x^1\sigma_x^2\sigma_y^3\sigma_y^4$	H_{18}
12	6.03396×10^{-2}	$\sigma_z^3\sigma_z^5$	H_4	44	-1.03458×10^{-2}	$\sigma_y^1\sigma_y^2\sigma_x^3\sigma_x^4$	H_{18}
13	6.28713×10^{-2}	$\sigma_z^1\sigma_z^5$	H_4	45	1.03458×10^{-2}	$\sigma_x^1\sigma_y^2\sigma_y^3\sigma_x^4$	H_{18}
14	5.64568×10^{-2}	$\sigma_z^1\sigma_z^4$	H_5	46	1.03458×10^{-2}	$\sigma_y^1\sigma_x^2\sigma_x^3\sigma_y^4$	H_{18}
15	6.03396×10^{-2}	$\sigma_z^4\sigma_z^6$	H_5	47	-2.84063×10^{-3}	$\sigma_x^3\sigma_x^4\sigma_y^5\sigma_y^6$	H_{19}
16	6.87743×10^{-2}	$\sigma_z^1\sigma_z^6$	H_5	48	-2.84063×10^{-3}	$\sigma_y^3\sigma_y^4\sigma_x^5\sigma_x^6$	H_{19}
17	5.36162×10^{-2}	$\sigma_z^2\sigma_z^4$	H_6	49	2.84063×10^{-3}	$\sigma_x^3\sigma_y^4\sigma_y^5\sigma_x^6$	H_{19}
18	6.87743×10^{-2}	$\sigma_z^2\sigma_z^5$	H_6	50	2.84063×10^{-3}	$\sigma_y^3\sigma_x^4\sigma_x^5\sigma_y^6$	H_{19}
19	7.06853×10^{-2}	$\sigma_z^4\sigma_z^5$	H_6	51	-5.90301×10^{-3}	$\sigma_x^1\sigma_x^2\sigma_y^5\sigma_y^6$	H_{20}
20	5.64568×10^{-2}	$\sigma_z^2\sigma_z^3$	H_7	52	-5.90301×10^{-3}	$\sigma_y^1\sigma_y^2\sigma_x^5\sigma_x^6$	H_{20}
21	6.28713×10^{-2}	$\sigma_z^2\sigma_z^6$	H_7	53	5.90301×10^{-3}	$\sigma_x^1\sigma_y^2\sigma_y^5\sigma_x^6$	H_{20}
22	7.06853×10^{-2}	$\sigma_z^3\sigma_z^6$	H_7	54	5.90301×10^{-3}	$\sigma_y^1\sigma_x^2\sigma_x^5\sigma_y^6$	H_{20}
23	-1.49854×10^{-3}	$\sigma_x^1\sigma_x^3$	H_8	55	-4.73898×10^{-3}	$\sigma_x^2\sigma_x^3\sigma_x^5\sigma_x^6$	H_{21}
24	-1.49854×10^{-3}	$\sigma_y^1\sigma_y^3$	H_8	56	-4.73898×10^{-3}	$\sigma_y^2\sigma_y^3\sigma_y^5\sigma_y^6$	H_{21}
25	1.13678×10^{-2}	$\sigma_x^2\sigma_x^4$	H_9	57	-4.73898×10^{-3}	$\sigma_x^2\sigma_y^3\sigma_y^5\sigma_x^6$	H_{21}
26	1.13678×10^{-2}	$\sigma_y^2\sigma_y^4$	H_9	58	-4.73898×10^{-3}	$\sigma_y^2\sigma_x^3\sigma_x^5\sigma_y^6$	H_{21}
27	1.04793×10^{-2}	$\sigma_x^1\sigma_z^2\sigma_x^3$	H_{10}	59	-4.73898×10^{-3}	$\sigma_x^1\sigma_z^2\sigma_z^3\sigma_x^4\sigma_y^5\sigma_y^6$	H_{22}
28	1.04793×10^{-2}	$\sigma_y^1\sigma_z^2\sigma_y^3$	H_{10}	60	-4.73898×10^{-3}	$\sigma_y^1\sigma_z^2\sigma_z^3\sigma_y^4\sigma_x^5\sigma_x^6$	H_{22}
29	1.04793×10^{-2}	$\sigma_x^2\sigma_z^3\sigma_x^4$	H_{11}	61	4.73898×10^{-3}	$\sigma_x^1\sigma_z^2\sigma_z^3\sigma_y^4\sigma_y^5\sigma_x^6$	H_{22}
30	1.04793×10^{-2}	$\sigma_y^2\sigma_z^3\sigma_y^4$	H_{11}	62	4.73898×10^{-3}	$\sigma_y^1\sigma_z^2\sigma_z^3\sigma_x^4\sigma_x^5\sigma_y^6$	H_{22}
31	-1.17598×10^{-3}	$\sigma_x^1\sigma_z^2\sigma_x^3\sigma_z^4$	H_{12}				
32	-1.17598×10^{-3}	$\sigma_y^1\sigma_z^2\sigma_y^3\sigma_z^4$	H_{12}				

For LiH molecules, we assume perfect filling of the two innermost $1s$ spin orbitals of Li and define the Hamiltonian on the basis of the $2s$ and $2p_x$ orbitals that are associated with Li and the $1s$ orbitals that are associated with H, for a total of six spin orbitals. After the JWT, we obtain a six-qubit Hamiltonian. We explicitly list the LiH Hamiltonian at the bound distance in Table III.

APPENDIX E: FINDING THE GROUND STATE OF H_2 ON THE SUPERCONDUCTING AND TRAPPED ION QPU

The two-qubit H_2 Hamiltonian (D3) contains four nonidentity terms, each corresponding to a nonunitary evolution operator when we apply the PITE,

$$\begin{aligned}\tilde{T}_1 &= \exp\big(-c_1\sigma_z^1\Delta\tau\big),\\ \tilde{T}_2 &= \exp\big(-c_1\sigma_z^2\Delta\tau\big),\\ \tilde{T}_3 &= \exp\big(-c_2\sigma_z^1\sigma_z^2\Delta\tau\big),\\ \tilde{T}_4 &= \exp\big(-c_3\sigma_x^1\sigma_x^2\Delta\tau\big).\end{aligned} \tag{E1}$$

In the tasks, we need to apply $\tilde{T}_1$, $\tilde{T}_2$, $\tilde{T}_3$, and $\tilde{T}_4$ on the work qubits in turn, as a cycle. At the end of each cycle, we need to measure the energy expectation value to show its convergence. We use the four types of quantum circuits shown in Figs. 9(a)–9(d) to implement $\tilde{T}_k$ with $k=1,2,3,4$, respectively. These circuits are composed of the following parts.

(i) Blue blocks show U and $U^\dagger$, which correspond to U_k and $U_k^\dagger$ in Fig. 1.

(ii) Orange blocks show the controlled-R_y gate, which corresponds to the controlled-R_y gate in Fig. 1.

(iii) Green blocks show the basis transformation. Theoretically, the quantum state in the experiments has the form $\cos(\phi/2)\,|00\rangle-\sin(\phi/2)\,|11\rangle$, where $0<\phi<\pi$, and usually ϕ is around the order of 10^{-3}–10^{-2}, the same as the measurement error. If we directly measure the work qubits on the ZZ basis, the probability of obtaining $|11\rangle$ would be significantly affected by the error. Therefore, we apply a basis transformation before the tomography, after which the state becomes $\frac{\cos(\phi/2)-\sin(\phi/2)}{\sqrt{2}}\,|00\rangle+\frac{\cos(\phi/2)+\sin(\phi/2)}{\sqrt{2}}\,|10\rangle$. Measuring the first qubit leads to 0 with probability of $p_0=[\cos(\phi/2)-\sin(\phi/2)]^2/2=(1-\sin\phi)/2$ and to 1 with probability of $p_1=(1+\sin\phi)/2$. Here p_0 and p_1 are around 0.4–0.6, much bigger than the measurement error and less affected by the error.

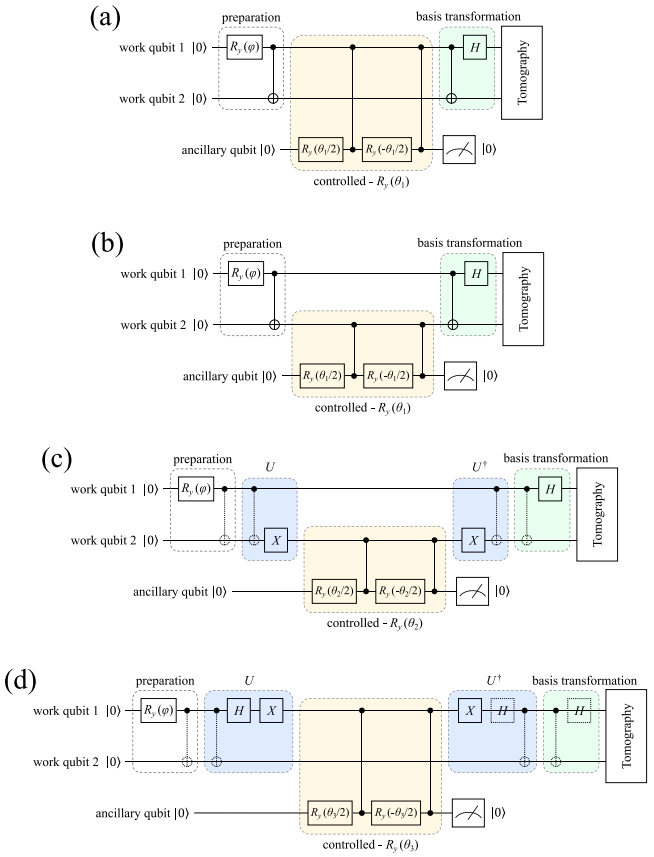

FIG. 9. Quantum circuits for applying PITE on H_2 molecules on the quantum cloud platforms, with the nonunitary evolution operators (a) $\tilde{T}_1$, (b) $\tilde{T}_2$, (c) $\tilde{T}_3$, and $\tilde{T}_4$. The quantum gates with dashed lines cancel each other out, so they are not carried out in the tasks.

(iv) White blocks show preparation and tomography. At the end of a Trotter step, we tomograph the quantum state of work qubits after basis transformation. Then we calculate the proper state numerically by reversing the basis transformation and prepare the state in the next quantum circuit as the input state. As the state only evolves in the real-coefficient subspace spanned by $|00\rangle$ and $|11\rangle$, the preparation only requires an R_y gate and a CNOT gate. The angular parameter ϕ of R_y can be obtained from the tomography result. Specifically, as we discussed in the preceding paragraph, we have $\sin\phi = 2p_1 - 1 = 1 - 2p_0 = p_1 - p_0$. Each tomography is repeated three times (with 2000 shots on superconducting QPUs and 1000 shots on trapped ion QPUs for each time). We calculate ϕ for each time and take their average value as the input parameter of the next Trotter step. For the first Trotter step, the input state is simply $|\Phi_{\mathrm{HF}}\rangle = |00\rangle$, i.e., the input parameter $\phi = 0$. In addition, after the tomography of the $\tilde{T}_4$ circuit, we also use the proper state to calculate the energy value $\langle E\rangle = \langle\Phi|\mathcal{H}_{\mathrm{H_2}}|\Phi\rangle$.

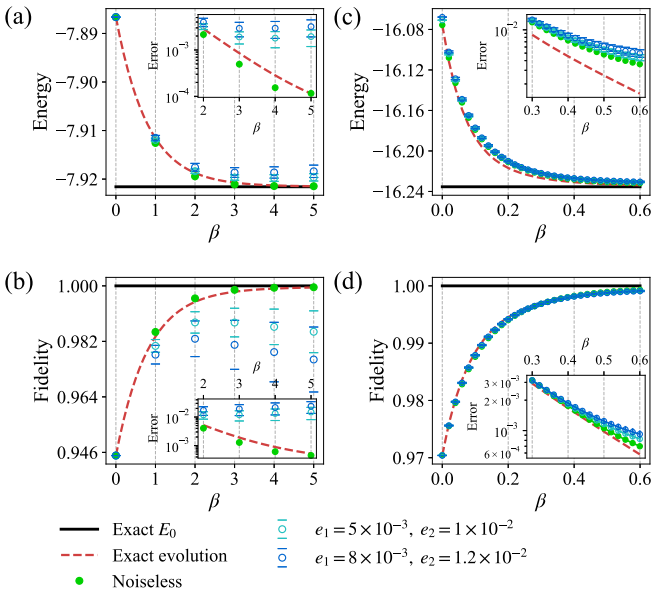

FIG. 11. Numerical simulation results of LiH and quantum Ising chain obtained from the PITE algorithm. (a) Energy values of LiH as a function of β. (b) Fidelity values of LiH as a function of β. The results in (a) and (b) are obtained at a fixed interatomic distance $R = 2.0$ Å. (c) Energy values of the Ising chain as a function of β. (d) Fidelity values of the Ising chain as a function of β. For the Ising chain, the parameters are chosen as $n = 10$, $J = 1$, $g = 1.2$, and $h = 0.3$. The black lines in (a) and (c) represent the exact ground-state energies obtained by diagonalization. The red dashed lines in [(a)–(d)] are results of exact imaginary-time evolution.

APPENDIX F: NUMERICAL SIMULATIONS USING GENERALIZED PITE

For the quantum Ising cyclic chain, we rewrite its Hamiltonian as $\mathcal{H} = \sum_{k=1}^{n} H_k$, with

$$H_k = -\left(\sigma_z^k \sigma_z^{k+1} + g\sigma_x^k + h\sigma_z^k\right) \tag{F1}$$

in the case where $J = 1$. Thus every H_k is a local operator acting on the kth and $(k+1)$th qubits. We can write the matrix

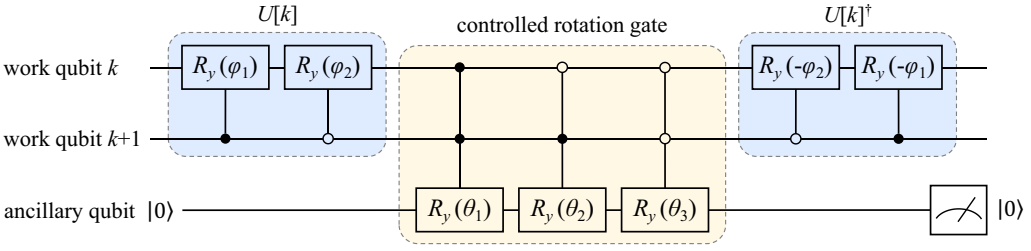

FIG. 10. Quantum circuit that implements $e^{-H_k\Delta\tau}$ for solving the quantum Ising model.

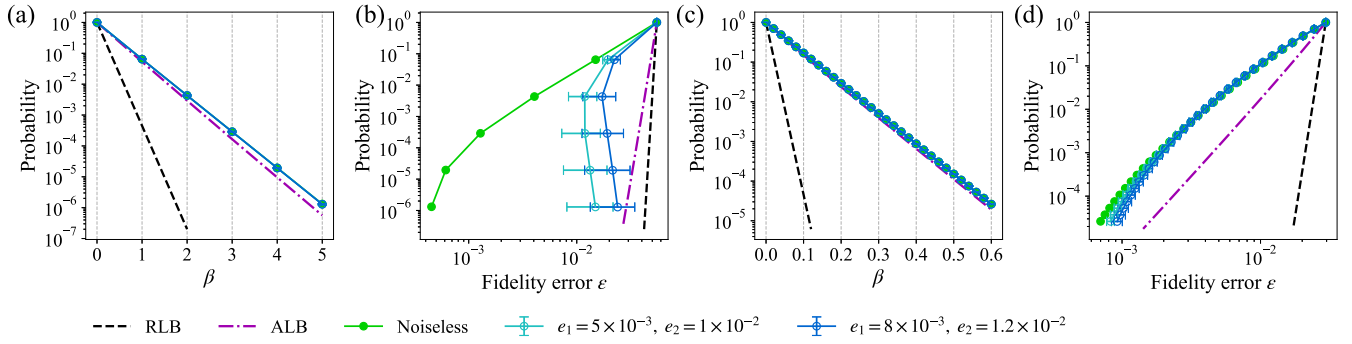

FIG. 12. Success probabilities of PITE in numerical simulations of LiH molecules and the quantum Ising chain. (a) Success probability of LiH as a function of the imaginary time β. (b) Success probability of LiH as a function of the output fidelity error ϵ. (c) Success probability of the Ising chain as a function of β. (d) Success probability of the Ising chain as a function of the output fidelity error ϵ. In (b) and (d) the initial states are at the top right side of the figures and evolve toward the bottom left side. For LiH, the RLBs and ALBs are calculated without the identity term of the Hamiltonian.

form of H_k in the two-qubit computational basis

$$H_k = -\begin{pmatrix} 1+h & 0 & g & 0 \\ 0 & -1+h & 0 & g \\ g & 0 & -1-h & 0 \\ 0 & g & 0 & 1-h \end{pmatrix}. \tag{F2}$$

Its eigenvalues are $\lambda_{0,3} = \mp\sqrt{g^2+(h+1)^2}$ and $\lambda_{1,2} = \mp\sqrt{g^2+(h-1)^2}$ and the corresponding eigenstates $|\lambda_{0,1,2,3}\rangle$ are also known. Following the procedure given in Sec. IV, we can use the quantum circuit shown in Fig. 10 to implement $e^{-H_k\Delta\tau}$, and the angles of the rotation gates are

$$\begin{aligned} \phi_1 &= \cos^{-1}\frac{1-h}{\sqrt{g^2+(h-1)^2}}, \\ \phi_2 &= \cos^{-1}\frac{-1-h}{\sqrt{g^2+(h+1)^2}}, \\ \theta_i &= 2\cos^{-1}(e^{-\Delta\tau(\lambda_i-\lambda_0)}), \quad i=1,2,3. \end{aligned} \tag{F3}$$

For the LiH molecule, the Hamiltonian has 62 Pauli terms (including the identity term). After neglecting the identity, we rearrange the other 61 terms and group them into 22 sets, with each set corresponding to a $H_{k'}$ as in the generalized PITE algorithm. When doing this, we follow the guidance of increasing $\sum_k \lambda_{k,0}$ (see details in Appendix C) and the principle that the eigensystems of every H_k should be efficiently known through classical computation. The grouping of the Pauli terms in the LiH Hamiltonian at its bound distance is shown in Table III, and the same grouping strategy is employed for other interatomic distances.

APPENDIX G: SIMULATION OF NOISES IN QUANTUM CIRCUITS

The quantum noise is described by the quantum channel

$$\mathcal{E}(\rho) = \sum_\nu \hat{E}_\nu \rho \hat{E}_\nu^\dagger, \tag{G1}$$

where ρ is the density matrix of the system and $\hat{E}_\nu$ are Kraus operators, satisfying

$$\sum_\nu \hat{E}_\nu^\dagger \hat{E}_\nu = I. \tag{G2}$$

For a single qubit in a quantum circuit, the main sources of quantum noise are qubit relaxation and dephasing, which correspond to the three Kraus operators shown in Eq. (11). For n-qubit cases, the number of Kraus operators is 3^n, and each Kraus operator can be described by $\hat{E}_{\nu'} \in \{\hat{E}_1, \hat{E}_2, \hat{E}_3\}^{\otimes n}$.

Moreover, we use another model of quantum noise. We consider all single-qubit gates as a rotation operation with respect to an axis, and the error is described as a random noise of the rotation angle which satisfies a normal distribution with the standard deviation e_1. For two-qubit gates, we consider their constructions as sequences of single-qubit gates and controlled-Z (CZ) gates. With a random noise, the CZ gate will become a C-phase gate whose matrix form is $\mathrm{diag}(1, 1, 1, e^{i\phi})$, where ϕ satisfies a normal distribution with the expectation value π and the standard deviation e_2. Using this model, we simulate the PITE algorithm in the cases of LiH molecules and the Ising chain. Figures 11 and 12 show the results of the simulation.

[1] L. Lehtovaara, J. Toivanen, and J. Eloranta, Solution of time-independent Schrödinger equation by the imaginary time propagation method, J. Comput. Phys. **221**, 148 (2007).

[2] C. V. Kraus and J. I. Cirac, Generalized Hartree-Fock theory for interacting fermions in lattices: Numerical methods, New J. Phys. **12**, 113004 (2010).

[3] F. Turro, A. Roggero, V. Amitrano, P. Luchi, K. A. Wendt, J. L. Dubois, S. Quaglioni, and F. Pederiva, Imaginary-time propagation on a quantum chip, Phys. Rev. A **105**, 022440 (2022).

[4] F. Verstraete, J. J. Garcia-Ripoll, and J. I. Cirac, Matrix product density operators: Simulation of finite-temperature and dissipative systems, Phys. Rev. Lett. **93**, 207204 (2004).

[5] S. R. White, Minimally entangled typical quantum states at finite temperature, Phys. Rev. Lett. **102**, 190601 (2009).

[6] S.-N. Sun, M. Motta, R. N. Tazhigulov, A. T. K. Tan, G. K.-L. Chan, and A. J. Minnich, Quantum computation of finite-temperature static and dynamical properties of spin systems using quantum imaginary time evolution, PRX Quantum **2**, 010317 (2021).

[7] J. Haah, R. Kothari, and E. Tang, *Proceedings of the 2022 IEEE 63rd Annual Symposium on Foundations of Computer Science, Denver* (IEEE, Piscataway, 2022), pp. 135–146.

[8] H. Kamakari, S.-N. Sun, M. Motta, and A. J. Minnich, Digital quantum simulation of open quantum systems using quantum imaginary-time evolution, PRX Quantum **3**, 010320 (2022).

[9] N. Okuma and Y. O. Nakagawa, Nonnormal Hamiltonian dynamics in quantum systems and its realization on quantum computers, Phys. Rev. B **105**, 054304 (2022).

[10] J. R. McClean and A. Aspuru-Guzik, Clock quantum monte carlo technique: An imaginary-time method for real-time quantum dynamics, Phys. Rev. A **91**, 012311 (2015).

[11] P. Czarnik, L. Cincio, and J. Dziarmaga, Projected entangled pair states at finite temperature: Imaginary time evolution with ancillas, Phys. Rev. B **86**, 245101 (2012).

[12] E. Stoudenmire and S. R. White, Minimally entangled typical thermal state algorithms, New J. Phys. **12**, 055026 (2010).

[13] R. P. Feynman, Simulating physics with computers, Int. J. Theor. Phys. **21**, 467 (1982).

[14] P. Benioff, The computer as a physical system: A microscopic quantum mechanical Hamiltonian model of computers as represented by turing machines, J. Stat. Phys. **22**, 563 (1980).

[15] Y. I. Manin, Computable and Uncomputable (Sovetskoe Radio, Moscow,1980).

[16] S. Lloyd, Universal quantum simulators, Science **273**, 1073 (1996).

[17] D. S. Abrams and S. Lloyd, Simulation of many-body Fermi systems on a universal quantum computer, Phys. Rev. Lett. **79**, 2586 (1997).

[18] A. Y. Kitaev, Quantum measurements and the Abelian stabilizer problem, arXiv:quant-ph/9511026.

[19] A. Aspuru-Guzik, A. D. Dutoi, P. J. Love, and M. Head-Gordon, Simulated quantum computation of molecular energies, Science **309**, 1704 (2005).

[20] R. Babbush, P. J. Love, and A. Aspuru-Guzik1, Adiabatic quantum simulation of quantum chemistry, Sci. Rep. **4**, 6603 (2014).

[21] M. A. Nielsen and I. L. Chuang, *Quantum Computation and Quantum Information* (Cambridge University Press, Cambridge, 2000).

[22] S. Gu, R. D. Somma, and B. Şahinoğlu, Fast-forwarding quantum evolution, Quantum **5**, 577 (2021).

[23] Z. Holmes, G. Muraleedharan, R. D. Somma, Y. Subasi, and B. Şahinoğlu, Quantum algorithms from fluctuation theorems: Thermal-state preparation, Quantum **6**, 825 (2022).

[24] C. Neill, T. McCourt, X. Mi, Z. Jiang, M. Y. Niu, W. Mruczkiewicz, I. Aleiner, F. Arute, K. Arya, J. Atalaya *et al.*, Accurately computing the electronic properties of a quantum ring, Nature (London) **594**, 508 (2021).

[25] S. McArdle, T. Jones, S. Endo, Y. Li, S. C. Benjamin, and X. Yuan, Variational ansatz-based quantum simulation of imaginary time evolution, npj Quantum Inf. **5**, 75 (2019).

[26] X. Yuan, S. Endo, Q. Zhao, Y. Li, and S. C. Benjamin, Theory of variational quantum simulation, Quantum **3**, 191 (2019).

[27] T. Jones, S. Endo, S. McArdle, X. Yuan, and S. C. Benjamin, Variational quantum algorithms for discovering Hamiltonian spectra, Phys. Rev. A **99**, 062304 (2019).

[28] S. Endo, J. Sun, Y. Li, S. C. Benjamin, and X. Yuan, Variational quantum simulation of general processes, Phys. Rev. Lett. **125**, 010501 (2020).

[29] M. Benedetti, M. Fiorentini, and M. Lubasch, Hardware-efficient variational quantum algorithms for time evolution, Phys. Rev. Res. **3**, 033083 (2021).

[30] Y.-X. Yao, N. Gomes, F. Zhang, C.-Z. Wang, K.-M. Ho, T. Iadecola, and P. P. Orth, Adaptive variational quantum dynamics simulations, PRX Quantum **2**, 030307 (2021).

[31] J. R. McClean, S. Boixo, V. N. Smelyanskiy, R. Babbush, and H. Neven, Barren plateaus in quantum neural network training landscapes, Nat. Commun. **9**, 4812 (2018).

[32] L. Bittel and M. Kliesch, Training variational quantum algorithms is NP-hard, Phys. Rev. Lett. **127**, 120502 (2021).

[33] M. Motta, C. Sun, A. T. K. Tan, M. J. O'Rourke, E. Ye, A. J. Minnich, F. G. S. L. Brandão, and G. K.-L. Chan, Determining eigenstates and thermal states on a quantum computer using quantum imaginary time evolution, Nat. Phys. **16**, 231 (2020).

[34] K. Yeter-Aydeniz, R. C. Pooser, and G. Siopsis, Practical quantum computation of chemical and nuclear energy levels using quantum imaginary time evolution and Lanczos algorithms, npj Quantum Inf. **6**, 63 (2020).

[35] Y. Huang, Y. Shao, W. Ren, J. Sun, and D. Lv, Efficient quantum imaginary time evolution by drifting real time evolution: An approach with low gate and measurement complexity, J. Chem. Theory Comput. **19**, 3868 (2023).

[36] H. Terashima and M. Ueda, Nonunitary quantum circuit, Int. J. Quantum Inf. **3**, 633 (2005).

[37] G.-L. Long, General quantum interference principle and duality computer, Commun. Theor. Phys. **45**, 825 (2006).

[38] S. Wei, H. Li, and G. Long, A full quantum eigensolver for quantum chemistry simulations, Research **2020**, 1486935 (2020).

[39] P. Lv, S. Wei, H.-N. Xie, and G. Long, QCSH: A full quantum computer nuclear shell-model package, Sci. China Phys. Mech. Astron. **66**, 240311 (2023).

[40] D. W. Berry, A. M. Childs, R. Cleve, R. Kothari, and R. D. Somma, Simulating Hamiltonian dynamics with a truncated taylor series, Phys. Rev. Lett. **114**, 090502 (2015).

[41] A. W. Schlimgen, K. Head-Marsden, L. M. Sager, P. Narang, and D. A. Mazziotti, Quantum simulation of open quantum systems using a unitary decomposition of operators, Phys. Rev. Lett. **127**, 270503 (2021).

[42] G. H. Low and I. L. Chuang, Optimal Hamiltonian simulation by quantum signal processing, Phys. Rev. Lett. **118**, 010501 (2017).

[43] Y. Dong, L. Lin, and Y. Tong, Ground-state preparation and energy estimation on early fault-tolerant quantum computers via quantum eigenvalue transformation of unitary matrices, PRX Quantum **3**, 040305 (2022).

[44] J. M. Martyn, Z. M. Rossi, A. K. Tan, and I. L. Chuang, Grand unification of quantum algorithms, PRX Quantum **2**, 040203 (2021).

[45] T. Liu, J.-G. Liu, and H. Fan, Probabilistic nonunitary gate in imaginary time evolution, Quantum Inf. Process. **20**, 204 (2021).

[46] T. Kosugi, Y. Nishiya, H. Nishi, and Y. Matsushita, Imaginary-time evolution using forward and backward real-time evolution with a single ancilla: First-quantized eigensolver algorithm for quantum chemistry, Phys. Rev. Res. **4**, 033121 (2022).

[47] H. F. Trotter, On the product of semi-groups of operators, Proc. Am. Math. Soc. **10**, 545 (1959).

[48] P. R. Chernoff, Note on product formulas for operator semigroups, J. Funct. Anal. **2**, 238 (1968).

[49] W. J. Hehre, R. Ditchfield, and J. A. Pople, Self-consistent molecular orbital methods. XII. Further extensions of Gaussian-type basis sets for use in molecular orbital studies of organic molecules, J. Chem. Phys. **56**, 5 (1972).

[50] J. I. Colless, V. V. Ramasesh, D. Dahlen, M. S. Blok, M. E. Kimchi-Schwartz, J. R. McClean, J. Carter, W. A. de Jong, and I. Siddiqi, Computation of molecular spectra on a quantum processor with an error-resilient algorithm, Phys. Rev. X **8**, 011021 (2018).

[51] A. Peruzzo, J. McClean, P. Shadbolt, M.-H. Yung, X.-Q. Zhou, P. J. Love, A. Aspuru-Guzik, and J. L. O'Brien, A variational eigenvalue solver on a photonic quantum processor, Nat. Commun. **5**, 4213 (2014).

[52] E. Farhi, J. Goldstone, and S. Gutmann, A quantum approximate optimization algorithm, arXiv:1411.4028.

[53] A. Gilyén, Y. Su, G. H. Low, and N. Wiebe, *Proceedings of the 51st Annual ACM SIGACT Symposium on Theory of Computing, Phoenix* (ACM, New York, 2019), pp. 193–204.

[54] A. T. Sornborger and E. D. Stewart, Higher-order methods for simulations on quantum computers, Phys. Rev. A **60**, 1956 (1999).

[55] C. Moler and C. Van Loan, Nineteen dubious ways to compute the exponential of a matrix, twenty-five years later, SIAM Rev. **45**, 3 (2003).

[56] C. Leadbeater, N. Fitzpatrick, D. Muñoz Ramo, and A. J. W. Thom, Non-unitary Trotter circuits for imaginary time evolution, arXiv:2304.07917.

[57] http://quafu.baqis.ac.cn/.

[58] http://github.com/ScQ-Cloud/pyquafu.

[59] https://ionq.com/quantum-systems/harmony.

[60] K. Wright, K. M. Beck, S. Debnath, J. M. Amini, Y. Nam, N. Grzesiak, J.-S. Chen, N. C. Pisenti, M. Chmielewski, C. Collins *et al.*, Benchmarking an 11-qubit quantum computer, Nat. Commun. **10**, 5464 (2019).